Medium-resolution spectroscopy of FORJ0332-3557: probing the interstellar medium and stellar populations of a lensed Lyman-break galaxy at z = 3.77

Rémi A. Cabanac, David Valls-Gabaud, Chris Lidman

To cite this version:

Rémi A. Cabanac, David Valls-Gabaud, Chris Lidman. Medium-resolution spectroscopy of FORJ0332-3557: probing the interstellar medium and stellar populations of a lensed Lyman-break galaxy at z = 3.77. Monthly Notices of the Royal Astronomical Society, 2008, 386 (4), pp.2065-2074. 10.1111/J.1365-2966.2008.13157.X . hal-00286614

HAL Id: hal-00286614
https://hal.science/hal-00286614v1

Submitted on 24 May 2017

Mon. Not. R. Astron. Soc. **386,** 2065–2074 (2008) doi:10.1111/j.1365-2966.2008.13157.x

Medium-resolution spectroscopy of FORJ0332−3557: probing the interstellar medium and stellar populations of a lensed Lyman-break galaxy at $z = 3.77$★

Rémi A. Cabanac,[1]† David Valls-Gabaud[2]† and Chris Lidman[3]†

[1]*LATT, Université de Toulouse, CNRS, 57 Avenue d'Azereix, 65000 Tarbes, France*
[2]*GEPI, CNRS UMR 8111, Observatoire de Paris, 5 Place Jules Janssen, 92195 Meudon Cedex, France*
[3]*ESO, Vitacura, Alonso de Cordova, 3107, Casilla 19001, Santiago, Chile*

Accepted 2008 February 27. Received 2008 February 26; in original form 2008 February 14

ABSTRACT

We recently reported the discovery of FORJ0332−3557, a lensed Lyman-break galaxy at $z = 3.77$ in a remarkable example of strong galaxy–galaxy gravitational lensing. We present here a medium-resolution rest-frame ultraviolet (UV) spectrum of the source, which appears to be similar to the well-known Lyman-break galaxy MS1512−cB58 at $z = 2.73$. The spectral energy distribution is consistent with a stellar population of less than 30 Ma, with an extinction of $A_v = 0.5$ mag and an extinction-corrected star formation rate $\mathrm{SFR_{UV}}$ of 200–300 $h_{70}^{-1}\,\mathrm{M_\odot\,a^{-1}}$. The Ly$\alpha$ line exhibits a damped profile in absorption produced by a column density of about $N_{\mathrm{H\,I}} = (2.5 \pm 1.0) \times 10^{21}\,\mathrm{cm^{-2}}$, superimposed on an emission line shifted both spatially (0.5 arcsec with respect to the UV continuum source) and in velocity space (+830 km s^{-1} with respect to the low-ionization absorption lines from its interstellar medium), a clear signature of outflows with an expansion velocity of about 270 km s^{-1}. A strong emission line from He II λ164.04 nm indicates the presence of Wolf–Rayet stars and reinforces the interpretation of a very young starburst. The metallic lines indicate subsolar abundances of elements Si, Al and C in the ionized gas phase.

Key words: gravitational lensing – galaxies: abundances – galaxies: high-redshift – galaxies: ISM – galaxies: starburst – galaxies: stellar content.

1 INTRODUCTION

Very few high-redshift galaxies ($z > 3$) have been observed spectroscopically at medium and high resolution until now because they are generally too faint for 8-/10-m class telescopes equipped with medium-resolution spectrographs. Over the past years the most successful technique to probe these high-redshift galaxies consisted in building composite spectra of low signal-to-noise ratio (S/N) samples (Shapley et al. 2001, 2003; Noll et al. 2004) and redshift-selected subsamples (Steidel, Pettini & Adelberger 2001; Ando et al. 2004). Very recently, high-redshift gamma-ray bursts have also led to a wealth of low-resolution spectral data on the interstellar medium (ISM) of young star-forming regions in high-redshift galaxies (Vreeswijk et al. 2004; Berger et al. 2006; Fynbo et al. 2006; Vreeswijk et al. 2006). From these composite samples a picture emerges of very young and massive stellar populations of 1/10th to 1/4th solar metallicities, dominated by ongoing star formation, with strong outflows, and a dusty component within abundant neutral gas.

As of today, only a handful of galaxies are bright enough to be studied spectroscopically at medium and high resolutions, and among them the most well-known example is MS1512−cB58 (cB58) (Pettini et al. 2000, 2002; Savaglio, Panagia & Padovani 2002, $z = 2.73$; look-back time = 11.4 Ga). A more recent example is the $6L_*$ $z = 5.5$ starburst (Dow-Hygelund et al. 2005) discovered in the field of a $z = 1.24$ galaxy cluster. The lensed galaxy FORJ0332−3557 (Cabanac et al. 2005, $z = 3.773$, look-back time = 12.1 Ga), which is the object of the present study, is the most recent addition to this select few.[1] Because the galaxy is magnified 13 times by a foreground lens at $z \sim 1$, it is bright enough to be observed at medium to high spectral resolution. We present here a 9-h-deep medium-resolution spectrum of the lensed galaxy taken with VLT/FORS2. The observations and data reduction are presented in Section 2 while Section 3 outlines the properties of the

---

★Based on observations made at the ESO VLT under programmes 74.A-0536 and 78.A-0240.

†E-mail: remi.cabanac@ast.obs-mip.fr (RAC); david.valls-gabaud@obspm.fr (DV-G); clidman@eso.org (CL)

[1] The advent of systematic surveys on wide fields is yielding many more potential candidates, see e.g. Bolton et al. (2006); Cabanac et al. (2007).

emission and absorption lines and in Section 4 we analyse the spectral energy distribution (SED) and the underlying stellar populations.

Throughout this paper we assume a flat FRW metric with $\Omega_\Lambda = 0.7, \Omega_\mathrm{M} = 0.3$ and a Hubble constant normalized at $h_{70} = 70\,\mathrm{km\,s^{-1}\,Mpc^{-1}}$. Following the recommendations adopted by the IAU, the letter 'a' is used for the non-SI unit of year.

2 OBSERVATIONS AND DATA REDUCTION

The observations were carried out with FORS2 on the European Southern Observatory VLT, under ESO programmes 74.A-0536 and 78.A-0240. A total exposure time of 8.71 h, split into 6×1495 s (1-arcsec slit) and 16×1400 s (0.8-arcsec slit), was obtained (see Table 1). We used the holographic grism 600RI (0.163 nm pixel^{-1}) together with the GG435 order-sorting filter, which results in resolving powers of 1200 and 1000 for the 0.8- and 1-arcsec slits, respectively. Since the 0.8- and 1-arcsec slits are slightly shifted with respect to each other in the focal plane, the resulting spectral coverage, 529.7–862.8 nm for the 1-arcsec slit and 501.1–832.5 nm for the 0.8-arcsec slit, differ slightly. The detector was the upgraded MIT 2×4096×2048 mosaic, which with the standard resolution collimator yields a physical scale of 0.126 arcsec pixel^{-1}. We oriented the slits north–south and centred them on the brightest part of the main arc (see Fig. 1). We used the standard 2 × 2 binned mode, which results in a final physical scale of 0.252 arcsec pixel^{-1} and a sampling of 4 and 3.2 pixels for the 1- and 0.8-arcsec slits, respectively. We placed the source on CCD1 (the upper northern chip), and used a 20-arcsec nod-on-slit strategy that allowed us to remove most sky artefacts.

The science data were taken during seven nights (two nights for 1-arcsec slit, five nights for 0.8 arcsec). The ESO standard calibration scheme delivers a set of bias, flat-field and wavelength calibration (from an He–Ar arc) frames for each night. We, then, subtracted master biases and divided by the 2D normalized master flat-fields. We evaluated the fringing contamination to be ca. 1 per cent peak-to-valley in the most sensitive part of the frames.

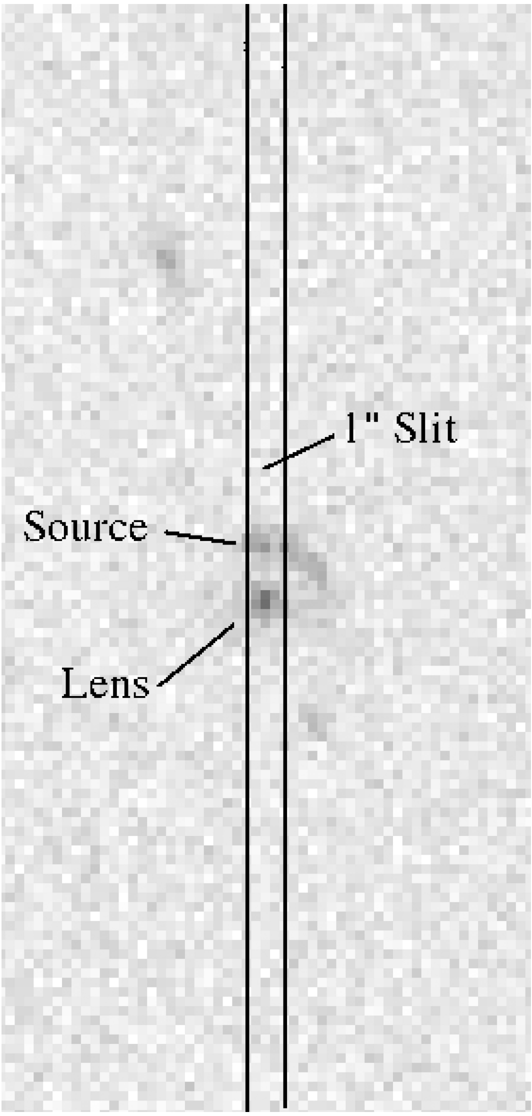

Figure 1. VLT/FORS2 acquisition frame (in the *R* band) and 1-arcsec-slit mask position on FORJ0332−3557: the central object is the lens at $z \sim 1$ and the top arc is the lensed LBG at $z \sim 3.77$.

Table 1. Description of spectroscopic data with *VLT*/*FORS2*.

Date UT time y-m-d h:m:s	Exposure time (s)	Airmass –	Seeing (arcsec)	Slit (arcsec)
2004-11-16 01:02:19	1495	1.446	0.56	1.0
2004-11-16 01:28:01	1495	1.326	0.55	1.0
2004-11-16 01:54:29	1495	1.231	0.65	1.0
2004-11-16 02:20:09	1495	1.161	0.76	1.0
2005-01-30 01:20:45	1495	1.103	0.50	1.0
2005-01-30 01:46:26	1495	1.154	0.54	1.0
2006-10-16 06:02:29	1400	1.028	0.66	0.8
2006-10-16 06:26:57	1400	1.020	0.53	0.8
2006-10-16 06:51:33	1400	1.021	0.61	0.8
2006-10-16 07:15:52	1400	1.031	0.50	0.8
2006-10-16 07:55:52	1400	1.068	0.73	0.8
2006-10-16 08:20:31	1400	1.104	0.61	0.8
2006-10-21 07:37:59	1400	1.070	0.48	0.8
2006-10-21 08:02:09	1400	1.106	0.61	0.8
2006-11-21 07:03:26	1400	1.266	0.85	0.8
2006-11-22 04:33:11	1400	1.023	0.85	0.8
2006-11-22 04:57:20	1400	1.036	0.89	0.8
2006-11-28 04:24:07	1400	1.030	0.54	0.8
2006-11-28 04:48:36	1400	1.048	0.63	0.8
2006-11-28 05:20:59	1400	1.087	0.50	0.8
2006-11-28 05:45:14	1400	1.130	0.57	0.8
2007-01-25 04:30:28	1400	1.916	0.67	0.8

We performed two independent reductions on the 1-arcsec slit data set. First, we reduced separately each science exposure and recombined the resulting 1D spectra after all calibrations. Secondly, we combined all science exposures using the FITS header World Coordinate info (WCS keywords) and removed the instrumental and sky artefacts on the combined 2D image before extracting and calibrating the source spectrum.

In the first method we used standard NOAO/IRAF routines in order to extract the trace with a fourth-degree Legendre polynomial in the dispersion direction, weighted by the spectrum variance perpendicular to the dispersion direction. We removed the sky emission from 1D modelling of the sky emission as measured on both sides of the trace. We then calibrated each extracted trace with the wavelength calibration frames (first-order cubic spline) respecting the source spectrum slit position. FORS2 flexures are very small and the final rms of ±0.02 nm derived for the wavelength frame was assumed to apply to the science exposures as well. All wavelengths were shifted to the heliocentric reference frame. Finally the combination of the resulting six 1D spectra (1-arcsec slit data; Table 1) was done using a median algorithm rejecting the minimum value and two maxima.

In the second method the sky subtraction was done using an optimal fitting while combining the 2D spectra. The wavelength calibration frames proved to be stable between the two nights (1-arcsec slit data; Table 1). Fig. 2 shows the resulting 2D frame after sky subtraction.

Both methods lead to a similar final S/N and wavelength calibration accuracies across the useful wavelength range. The second method seems to lead to a slightly larger convolution of the observed linewidths than the first method. We reduced the 0.8-arcsec slit data using the second method only.

An important calibration step is the instrument response correction. The response curve of FORS2 was computed from spectrophotometric standard observations (LTT1788 and LTT2415 using a MOS 5-arcsec slit). Because the 0.8- and 1-arcsec slits are shifted with regards to the MOS slit, the wavelength range of the standard covers a slightly different range. We extrapolated the response curve linearly in the missing regions.

A final step was required to remove the contribution of the elliptical galaxy that produces the gravitational lens effect on the 2D spectrum of the source. We used two methods, which gave similar results. First, we subtracted the contribution of the lens measured on the southern profile at a symmetrical angular distance. Secondly, we measured the dominant IR contribution of the lens over the arc and subtracted the best-fitting SED normalized to that contribution (cf. Section 4).

3 EMISSION AND ABSORPTION LINES

3.1 Source redshift

In the low-resolution discovery spectrum (Cabanac et al. 2005) we estimated a source redshift of $z = 3.773 \pm 0.003$ from a few strong interstellar lines. The improved S/N obtained here (continuum peak S/N $\sim$ 15) allows us to measure here a revised systemic redshift of $z_{\rm LIS} = 3.7723 \pm 0.0005$, using 11 stronger detections of five atomic species: C, O, Al, Si and Fe, and excluding uncertain identifications and blended lines (see Table 2). We marginally detect two important photospheric lines O IV λ134.33) and S V λ150.18 (see Fig. 2). Hence we can only make a very tentative estimate of a possible velocity offset between the photospheric lines and the low-ionization ISM lines of about $+110 \pm 30\,{\rm km\,s^{-1}}$. This is about half the value inferred in cB58 of $+210\,{\rm km\,s^{-1}}$ (Pettini et al. 2000, 2002).

3.2 The Lyα lines

Fig. 2 shows the 2D spectrum and the associated 1D spectrum normalized to the continuum. Bluewards of Lyα the spectrum is poorly defined mostly because of foreground hydrogen absorption, and the continuum has been assumed to be located at the peaks of the spectrum. We also added the low-resolution VLT/FORS2 spectrum at wavelengths shorter than 110 nm (Cabanac et al. 2005). The Lyα, Lyβ and Lyγ absorption features are conspicuous, and unresolved Lyδabsorption is detected as well.

Fig. 3 zooms on the region around Lyα. A faint emission peak at $\Delta v = +830\,{\rm km\,s^{-1}}$ of the Lyα absorption centroid and $\sim 2 \pm 0.5$ pixels (0.51 ± 0.13 arcsec) north of the continuum emission is clearly visible. This feature can be interpreted either as a very bright H II region in the periphery of the main galaxy, or, more probably, as the signature of an expanding outflow. Assuming that the results of detailed 3D Monte Carlo Lyα radiative transfer codes Verhamme, Schaerer & Maselli (2006) (where the Lyα emission is produced by an expanding shell that is being ionized) can be applied to this case, we can infer that the expansion velocity of the shell that gives rise to the Lyα emission is constrained to be between $v_{\rm exp} \sim \Delta v \sim 800\,{\rm km\,s^{-1}}$ (low column density case) and $v_{\rm exp} \sim \Delta v/3 \sim 270\,{\rm km\,s^{-1}}$ (large column density case). It is therefore essential to measure the H I column density in this context.

If we assume that the Lyα absorption can be fitted by a damped Voigt profile,[2] we derive a column density of $N_{\rm H\,I} = (2.5 \pm 1.0) \times 10^{21}\,{\rm cm^{-2}}$. Fig. 4 shows the best-fitting damped Voigt profile and errors, along with the emission profile in velocity space obtained when the absorption profile is subtracted. The column density is remarkably large, about four times larger than in MS1215−cB58 (Pettini et al. 2002; Savaglio et al. 2002). If we adopt the model of an expanding shell at constant velocity (Verhamme et al. 2006), this column density still implies a large expansion velocity of about $v_{\rm exp} \sim 270\,{\rm km\,s^{-1}}$, similar to the one found in cB58 (Schaerer & Verhamme 2008), and at the upper end of the Lyman-break galaxies (LBGs) (Shapley et al. 2003) if they do have large H I column densities. It is remarkable that in spite of the very large column densities, such strong Lyα emissions are detected, confirming that the ISM is very clumpy, yielding smaller effective optical depths which are very similar to the ones inferred in the low-redshift starbursts (Valls-Gabaud 2003), and allowing many Lyα photons to escape.

The neutral gas content derived with Voigt profile fitting is fully consistent with the neutral gas content derived independently from the analysis of stellar populations (Section 4) with the gas-to-dust ratio taking Milky Way (MW) or Large Magellanic Cloud (LMC) values, but is ∼5–10 times smaller than the values observed in the Small Magellanic Cloud (SMC).

3.3 The He II λ164.04 nm emission line: the signature of very massive stars

A broad emission feature at 164.04 nm is seen in Fig. 2 at a redshift of $z = 3.7738$ consistent with other faint photospheric features. We associate this feature with the well-known He II emission produced by Wolf–Rayet stars. Although not present in cB58, this feature has already been detected in absorption in young LBGs (Shapley et al. 2001, cf. figs 15 and 16), and in emission in the composite LGB spectrum of Shapley et al. (2003) but the origin of the feature cannot be asserted by the authors because the composite spectrum mixes a wide range of stellar populations and ages. If FORJ0332−3557 is similar to other LBGs, it belongs to the strongly absorbed Lyα quartile, and the case for a very young stellar population (∼5 Ma) of massive stars is strong. The He II feature of Fig. 2 shows the typical asymmetric profile produced by strong stellar outflows of the evolved descendants of O stars more massive than $M > 20$–$30\,{\rm M_{\odot}}$. The equivalent width W_0(He II) yields the ratio of WR to O stars following Schaerer & Vacca (1998),

$$\log\left[\frac{\rm WR}{\rm WR+0}\right] = (-2.83 \pm 0.03) + (1.52 \pm 0.05)\log[W_0({\rm He\,II})], \quad (1)$$

---

[2] This is clearly a rough approximation since the spectrum comes from the integrated light of the source and there are photons that are scattered into the line of sight. Hence the profile cannot be a pure absorption profile, and the inferred column density is just indicative.

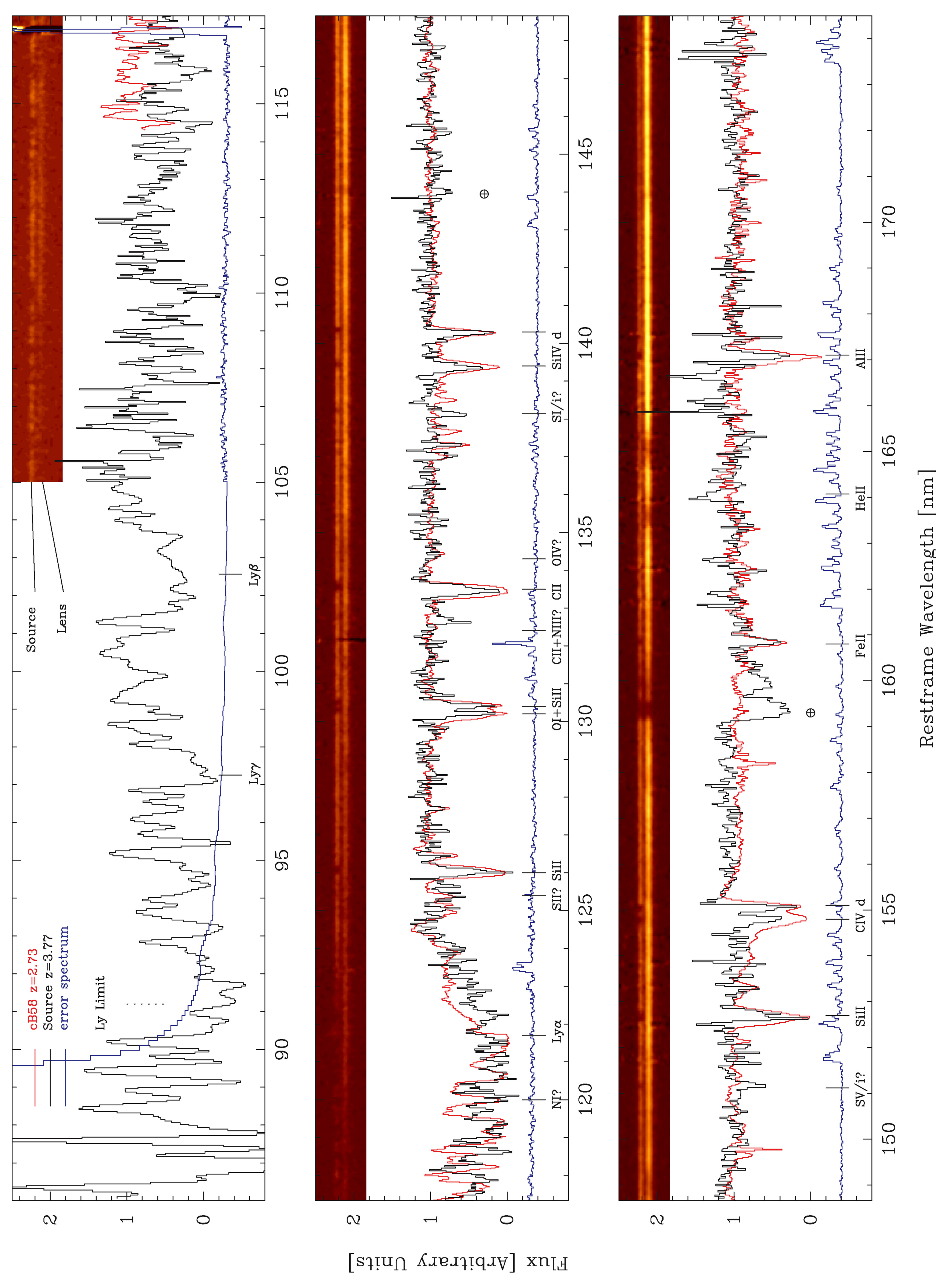

Figure 2. Continuum-normalized rest-frame UV spectrum of FORJ0332−3557 (black solid line), superimposed on its error spectrum (blue solid line, offset for clarity) and the spectrum of the $z = 2.73$ lensed galaxy cB58 (red solid line). The 2D spectrum of the source, part of a compact lensing configuration, is also shown on the top.

Table 2. Interstellar absorption lines.

Ion	$\lambda_{\rm vac}^{\rm lab}$ (nm)	$\lambda_{\rm vac}^{\rm obs}$ (nm)	Redshift	$W_0{}^a$ (nm)	f	$\log N^b$ (cm^{-2})	$[{\rm X/H}]_\odot{}^c$	Comments
H I Lyγ	97.254	–	–	$1.50 \pm 0.30^{+0.20}_{-0.10}$	0.0290	–	–	
H I Lyβ	102.57	–	–	$2.10 \pm 0.80^{+0.80}_{-0.60}$	0.07912	–	–	
H I Lyα	1215.7	–	–	–	0.4164	21.4 ± 0.2	–	
He II	164.04	783.09	3.7738	$-0.22 \pm 0.01^{+0.02}_{-0.02}$	–	–	–	WR feature
C II	133.45	637.01	3.7732	$0.21 \pm 0.03^{+0.03}_{-0.02}$	0.1278	15.019 ± 0.10	> -2.8	Blended with C II*λ133.57
C IV	154.82	738.74	3.7716	$0.10 \pm 0.03^{+0.06}_{-0.03}$	0.1908	14.40 ± 0.21	> -3.6	
C IV	155.08	740.00	3.7718	$0.19 \pm 0.05^{+0.02}_{-0.02}$	0.09522	14.97 ± 0.25	> -3.0	Sky contamination
N I?	~120	572.70	3.7718	$0.36 \pm 0.18^{+0.08}_{-0.05}$	0.04023	15.84 ± 0.25	-1.6?	Triplet N Iλ 119.95 120.02 120.07
N III?	132.43	632.24	3.7741	–	–	–	–	Blended with C II λ132.39
O I	130.22	621.31	3.7714	$0.15 \pm 0.03^{+0.05}_{-0.03}$	0.04887	15.30 ± 0.17	> -3.0	Blended with Si II λ130.44
O IV	134.34	641.27	3.7735	$0.14 \pm 0.01^{+0.05}_{-0.03}$	–	–	–	Photospheric
Al II	167.08	797.41	3.7726	$0.19 \pm 0.02^{+0.07}_{-0.03}$	1.833	13.62 ± 0.22	> -2.5	Sky contamination
S I/i?	138.16	659.29	3.7719	$0.11 \pm 0.01^{+0.03}_{-0.02}$	–	–	–	
S II/i?	125.38	598.57	3.7740	$0.12 \pm 0.02^{+0.04}_{-0.05}$	0.01088	15.90 ± 0.15	-1.1?	
S II/i?	125.95	601.31	3.7742	$0.19 \pm 0.04^{+0.03}_{-0.02}$	0.01624	–	–	Blended with Si II λ126.04
S V?	150.18	716.39	3.7741	$0.3 \pm 0.03^{+0.04}_{-0.2}$	0.00545	–	–	Photospheric
S II/i?	151.12	721.43	3.7740	$0.07 \pm 0.01^{+0.02}_{-0.02}$	–	–	–	Blended with Si II λ151.21
Si II	126.04	601.84	3.7749	$0.19 \pm 0.04^{+0.03}_{-0.02}$	1.007	14.13 ± 0.11	> -2.8	Blended with S II λ125.95
Si II	130.47	622.49	3.7710	$0.16 \pm 0.01^{+0.06}_{-0.03}$	0.094	15.05 ± 0.37	-1.9?	Blended with O I λ130.22
Si II	152.67	728.39	3.7710	$0.24 \pm 0.03^{+0.02}_{-0.02}$	0.130	14.96 ± 0.11	> -2.0	
Si II*?	153.34	731.40	3.7697	$0.04 \pm 0.01^{+0.01}_{-0.01}$	0.132	14.20 ± 0.10	-2.8?	
Si IV	139.38	665.09	3.7718	$0.19 \pm 0.03^{+0.03}_{-0.02}$	0.5140	14.33 ± 0.10	> -2.6	
Si IV	140.28	669.38	3.7718	$0.21 \pm 0.03^{+0.04}_{-0.02}$	0.2553	14.66 ± 0.12	> -2.3	Blended with S Iλ140.15?
Fe II	160.84	767.68	3.7728	$0.12 \pm 0.02^{+0.01}_{-0.02}$	0.058	14.95 ± 0.11	-2.0	

[a] Errors are given as statistical (± photon noise) and systematic (± systematic uncertainty in location of the continuum). [b] Lower limits based on the assumption of an optically thin medium. [c] Assuming solar abundances from Asplund, Grevesse & Sauval (2005).

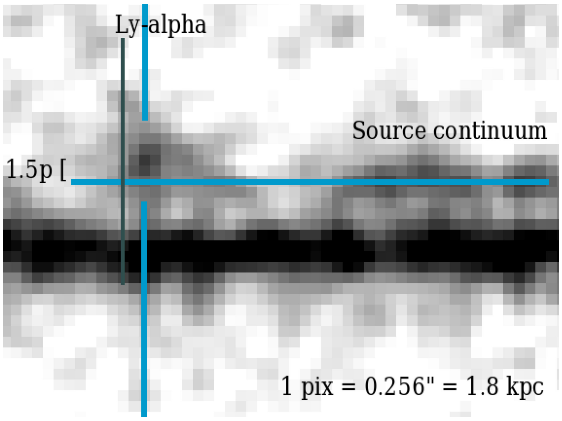

Figure 3. Zoom on the 2D spectrum around Lyα, showing the spatial offset of ~2 ± 0.5 pixels (0.51 ± 0.13 arcsec) and the velocity shift of $\Delta v = +830\,{\rm km\,s^{-1}}$, indicative of outflows (121.567 nm position is the narrow green vertical line). The lower trace is the spectrum of the elliptical galaxy that produces the gravitational lensing effect.

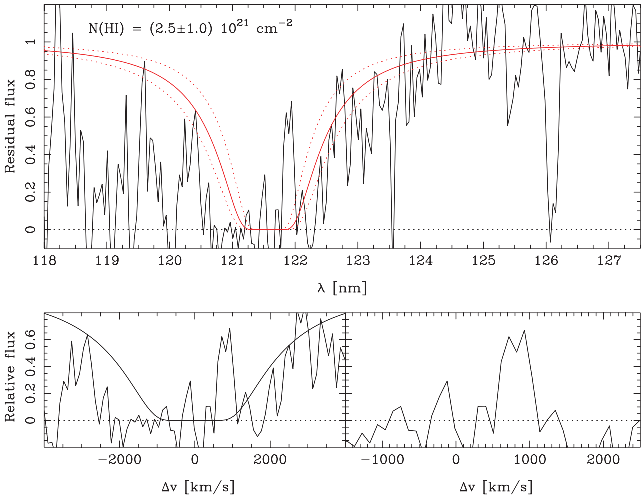

Figure 4. The best-fitting Voigt profile corresponding to a column density of $(2.5 \pm 1) \times 10^{21}\,{\rm cm}^{-2}$ (solid and red dotted lines) is shown on the rest-frame spectrum (top frame). The bottom frames show the same fit in velocity space Δv. On the panel at the bottom right-hand side the model is subtracted out of the spectrum, showing a conspicuous emission feature peaking at $\sim 830\,{\rm km\,s^{-1}}$. This feature is also offset spatially by 2 pixels (ca. 0.5 arcsec) from the main UV continuum emitting source (see Fig. 3).

which for $W_0({\rm He\,II}) = 0.22 \pm 0.02$ nm implies a ratio O/WR = 5 ± 1. In turn, this value sets a strong age limit on the stellar population of $\lesssim$6 Ma rather independently of metallicity (Cerviño & Mas-Hesse 1994; Schaerer 2003). Stochastic effects due to the sampling of the stellar mass function (e.g. Cerviño & Valls-Gabaud

2003; Cerviño et al. 2003) imply that only the most recent burst can be dated through this short-lived feature.

3.4 Interstellar absorption lines

The spectrum of FORJ0332−3557 shows characteristic absorption lines from starburst galaxies. They are summarized in Table 2. The medium-resolution spectrum of the LBG cB58 Pettini et al. (2000) is shown in Fig. 2 in red, superimposed on our source, for a direct comparison of the interstellar features. It is immediately obvious that the FORJ0332−3557 source is qualitatively similar to cB58.

All common interstellar absorptions are found in FORJ0332−3557. The strong absorption features include low-ionization lines associated with neutral gas (Si II λλλ126.04, 130.47, 152.67, C II λ133.45, O I λ130.22, Al II λ167.08, Fe II λ160.84) and high-ionization lines associated with a hot gas phase (Si IV λλ139.38, 140.28, C IV λλ154.82, 155.08). Table 2 lists the ion line identification, vacuum rest-frame wavelength $\lambda_{\mathrm{vac}}^{\mathrm{lab}}$, observed wavelength $\lambda_{\mathrm{vac}}^{\mathrm{obs}}$, redshift z, rest-frame equivalent width W_0, oscillator strengths f, column density, ion abundance with respect to solar $[\mathrm{X/H}]_\odot$ and comments. Additional uncertain identifications are question marked, the lines noted 'i?' might belong to interlopers at unknown redshift(s). We emphasize that the derived W_0 are very sensitive to both sky subtraction and continuum normalization, hence the systematic errors caused by the continuum normalization have tentatively been computed and are shown to be close to photon counting errors, while the sky subtraction error is much more difficult to quantify. As a sanity check, we computed the equivalent widths of absorption lines in the spectrum of cB58 and found our measurements to be fully consistent with those published by Pettini et al. (2002).

No nebular emission lines are detected in the present spectrum other than He II λ164.04nm (Section 3.3). A weak detection of C III] λ 190.87 seen on a previous spectrum (Cabanac et al. 2005) suggests that contamination of the high-ionization lines by nebular emission is present but small. P Cygni profiles are visible on C II λ133.45, and C IV λ155.08.

There are several ways to derive the abundances in the ISM of distant galaxies (Spitzer 1978; Pettini et al. 2002; Savaglio et al. 2002). Ideally one should build a curve of growth by fitting Voigt profiles and Doppler parameters b for all ions independently. Because the resolution of our observed spectrum is just under the resolution one needs for Voigt profile fitting, and is penalized by a low S/N, most of the strong lines appear saturated, and most weak lines are dominated by noise.

A careful analysis of the ISM metallicity goes beyond the present paper and will be done elsewhere. Here we present only qualitative arguments on the curve of growth, and Doppler parameters b. Assuming that the ISM in FORJ0332−3557 is optically thin, one can infer lower limits to column densities, $\log(N\ [\mathrm{cm}^{-2}])$, and abundances (given in Table 2) by taking the optically thin approximation

$$\log N\ (\mathrm{cm}^{-2}) = 19.053 + \log\left[\frac{W_\lambda}{\lambda^2 f}\right], \tag{2}$$

where f is the line oscillator strength. The equivalent width, W_λ, and the wavelength, λ, are in nm. A tentative curve of growth indicates that the ion abundances could be 2–3 dex larger for a Doppler parameter of $b = 50\,\mathrm{km\,s^{-1}}$. In this context, the most constraining line, besides Si II*λ153.3 which may be blended, is FeIIλ160.8, which appears unsaturated and whose small equivalent width is similar to the one measured in cB58 and would yield $b \sim 60\,\mathrm{km\,s^{-1}}$, similar to the $b \sim 70\,\mathrm{km\,s^{-1}}$ reported in cB58 (Pettini et al. 2002).

Compared to cB58, FORJ0332−3557 W_0 are lower by factors of 2–3 (C IVλλ155.08, 155.08, Al IIλ167.08, O Iλ130.22) to a factor of 1–1.2 (Si IVλλ139.38, 140.28, Fe IIλ160.84). More detailed analyses on elemental abundances and depletion in the ISM of FORJ0332−3557 will be presented elsewhere.

4 STELLAR POPULATIONS

After analysing the absorption and emission lines here we study the properties of the continuum, using recent stellar synthesis codes, which, for the first time, predict high-resolution spectra of starburst populations. We used both STARBURST99 (Leitherer et al. 1999; Vázquez & Leitherer 2005) and SED@ (Buzzoni 1989; Cerviño et al. 2002; Cerviño & Luridiana 2004) in an attempt to derive plausible combinations of ages, metallicities and extinctions by dust from the FORJ0332−3557 ultraviolet (UV) spectrum (Fig. 2).

4.1 Spectra predicted by STARBURST99

We build two series of STARBURST99 spectra using (1) an IMF with a Salpeter slope from 1 to 100 M$_\odot$,[3] (2) a self-consistent association of low-metallicity tracks with LMC/SMC atmospheric stellar templates and (3) solar metallicity tracks with galactic atmospheric stellar templates, from ages 0.01 to 50 Ma, for metallicities Z of 0.001 (1/20 Z$_\odot$), 0.004 (1/5 Z$_\odot$), 0.008 (2/5 Z$_\odot$) and 0.020 (Z$_\odot$). All STARBURST99 models were fitted to the spectrum of Fig. 2, pre-filtered with a Savitsky–Golay filter (conserving the equivalent width, FWHM and line profiles), to the same resolution as the STARBURST99 synthetic templates. The region below 123 nm was excluded from the fits, because the source is heavily contaminated by foreground interlopers. For solar metallicities, STARBURST99 high-resolution atmospheric templates go up to 180 nm, but only 160 nm for subsolar SMC/LMC metallicities. Only the highly ionized absorption lines were considered for the fitting, to avoid excessive interstellar contamination. An additional range of wavelengths (near 137 and 144 nm) was excluded due to telluric contamination. The regions included in the fit are shown as solid lines in Fig. 5. Different sets of constraints can be derived by fitting the line equivalent widths of the normalized spectrum and by fitting the shape of the spectrum continuum. Fig. 5 compares the best-fitting models with the normalized spectrum for two extreme scenarios of star formation: (i) a single burst of star formation (bottom) and (ii) a continuous SFR (top). The best-fitting models for $Z = 0.004$ have ages of 8 Ma (single burst) and 29 Ma (constant SFR). The age of the best-fitting models is found to be insensitive to metallicity in the case of single bursts. In the case of a constant SFR, increasing the metallicity tends to increase the age of the best-fitting model: 29 Ma at $Z = 0.001$, >49 Ma at $Z = 0.008$, and more than 50 Ma at $Z = 0.02$. We explored solar metallicity models with ages of 200 Ma and although the reduced χ^2 decreased slightly the highly ionized absorption lines did not get deeper significantly. The reduced χ^2 shows that constant SFR models become insensitive to age above 20 Ma, whereas single burst models appear to isolate a well-defined small region (6–9 Ma). However, neither of these scenarios can reproduce the observed depth of the absorption lines, which probably argues for interstellar origin for the highly ionized lines. Finally, the single

---

[3] Tests where the upper stellar mass cut-off of the IMF is reduced to 30 M$_\odot$ give very similar best-fitting ages.

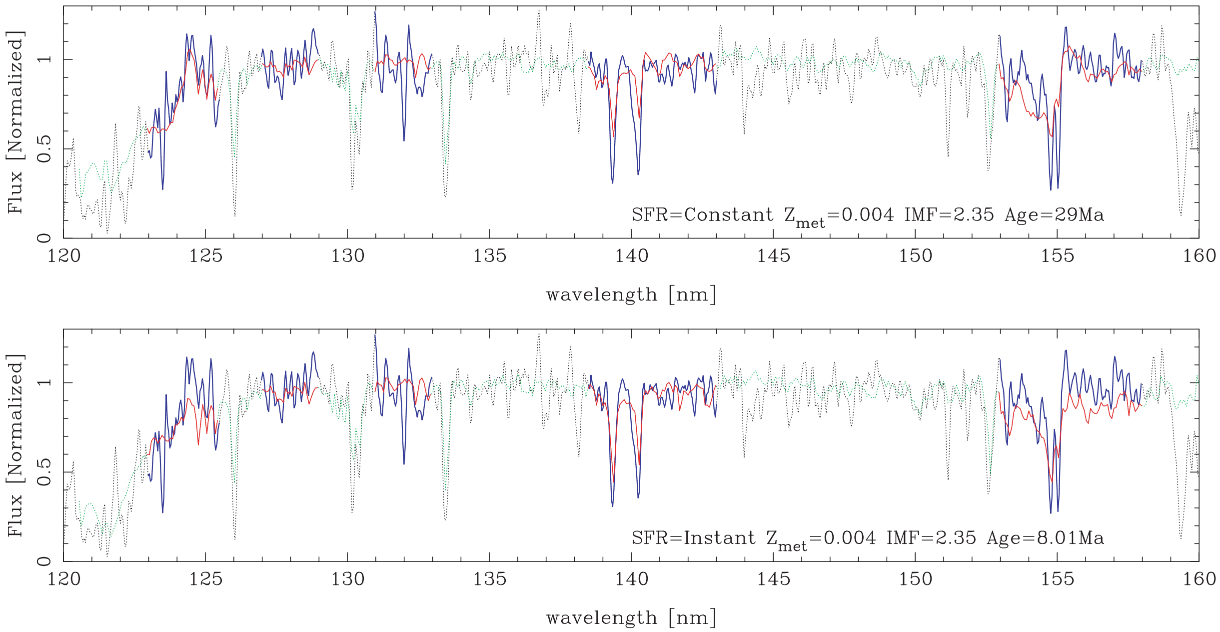

Figure 5. The best-fitting STARBURST99 models (red lines) are overlaid on the normalized spectrum of FORJ0332−3557 source (blue line) for two extreme scenarios of star formations with a Salpeter IMF from 1–100 $M_\odot$, at a metallicity $Z = 0.004$ ($1/5\,Z_\odot$). The parts of the spectrum excluded of the fit are shown as dotted lines (see text). The top frame shows a constant SFR for 29 Ma. Ages older than 20 Ma are strongly favoured. The bottom frame shows an 8-Ma-old instantaneous burst of star formation. No model (at any available metallicities ($1/20 - 1\,Z_\odot$) can reproduce the observed depths of the lines. For a constant SFR, larger metallicities produce older ages (29 Ma at $Z = 0.001$, >49 Ma at $Z = 0.008$). Instantaneous burst models tend to produce deeper lines while constant SFR models tend to better fit the observed P Cygni profiles of C IVλ155.08 nm.

burst scenario seems to produce slightly deeper absorption lines, whereas the constant SFR scenario better fits the P Cygni profiles of C IV$\lambda\lambda$155.08, 155.08 nm and the red side of Lyα. We also tested different stellar wind models without any significant differences.

4.2 Spectra predicted by SED@

The stellar population synthesis code SED@ is included in the Legacy Tool project of the Violent Star Formation Network[4] (Buzzoni 1989; Cerviño et al. 2002; Cerviño & Luridiana 2004). It computes UV spectra with the highest resolution currently available, consistently computing the errors introduced by a limited number of bright stars in a small burst (this effect can probably be neglected in our case unless the lens amplifies a single star-forming region within the source). We use a series of instantaneous burst models from 0 to 10 Ga, a Salpeter IMF, and Geneva stellar tracks at four metallicities: Z of 0.001 ($1/20\,Z_\odot$), 0.004 ($1/5\,Z_\odot$), 0.008 ($2/5\,Z_\odot$) and 0.020 ($Z_\odot$). As in the previous section, we treat independently the constraints coming from the normalized UV absorption features, and the overall photometric SED of the source. For the UV spectrum fitting, we isolate the strongly ionized absorption features containing most of the signal and exclude the weakly ionized features dominated by interstellar features, using the wavelength intervals 120–125, 127–129, 131–133, 134–143, 145–152 and 153–158 nm. We normalize each interval to the continuum by dividing each wavelength bin by the linear interpolation between the two extreme values of the interval. We compute the reduced χ^2 between the templates and the source UV spectrum for a grid of extinctions ($0 < A_v < 1$) and ages (1–1000 Ma). The photometric SED of the templates are integrated over the instrumental transmission curves (filter + telescope + CCD detector) given by VLT/FORS1 (B, v and R_C bands) and VLT/ISAAC (J, H, K_S bands) manuals, normalized to VEGA magnitude using Kurucz's solar model (Castelli & Kurucz 1994). Fig. 6 shows the resulting reduced χ^2 contours. Ages are along the horizontal axis (steps of 1 Ma from 0 to 10 Ma, steps of 5 Ma from 10 to 100, steps of 100 from 100 Ma and older ages). The extinction A_v is given on the vertical axis. The left-hand panel shows the contours of χ^2 values obtained in the fitting of the UV features described above (the contour levels are given at 1, 3 and 5 per cent above the value of the minimum χ^2). The central panel shows the contours obtained in the fitting of the photometric SED (contour levels at 1.5, 3 and 5 times the minimum χ^2), while the right-hand panel shows the combined constraints from both the overall SED and the UV features (contour levels at 1, 3 and 10 per cent above the minimum χ^2). The left-hand frame shows a complete degeneracy in extinction, as expected since we normalize the continuum and the UV is no longer sensitive to extinction. The central panel shows the well-known degeneracy between age and extinction but clearly shows a tendency to prefer young ages with higher extinction, rather than older ages with small extinctions. It should be noted that the χ^2 of the UV fitting alone shows a minimum at $Z = 0.004$, whereas the χ^2 of SED fitting alone favours the smallest metallicity models $Z = 0.001$. The combined set leads to $Z = 0.008$ (Fig. 6) but it is clearly not a very constraining result due the degeneracies involved.[5] Because the two sets of constraints are independent and almost orthogonal, the combined χ^2 shown in the right-hand panel of Fig. 6

---

[4] See the SED@ online Reference Manual at http://www.iaa.es/ñcs/sed@/index.html for more information.

[5] See e.g. Schaerer & Pelló (2005) for other examples of degeneracies in the SED fitting of high-z galaxies.

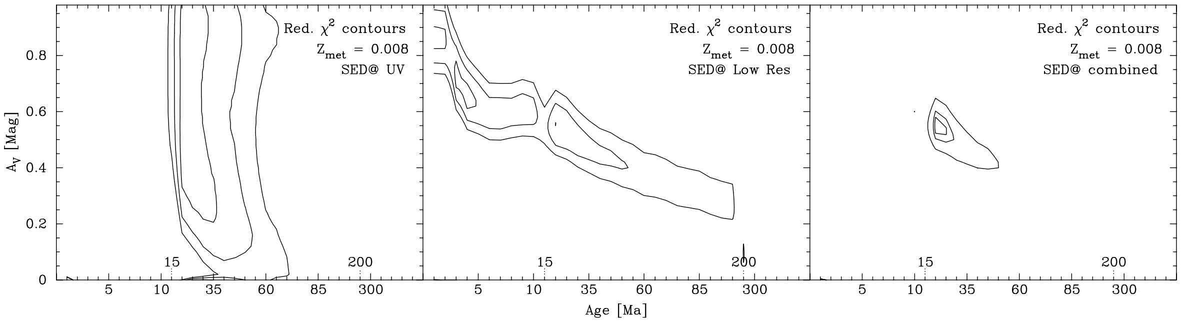

Figure 6. Reduced χ^2 contours are given for the best-fitting $Z = 0.008$ SED@ models for a grid of ages and extinctions. The contour levels are arbitrarily chosen to be 1, 3 and 10 per cent of the reduced χ^2 minimum, to outline the trends. The left-hand panel shows the contours derived for a continuum-normalized set of deep absorption lines alone (cf. text), the centre panel shows the constraints derived from the photometric colours alone, and the right-hand panel shows the combined contours of the two independent sets taken together. The optimal parameter set is age = 20 ± 5 Ma, $A_v = 0.55 \pm 0.02$.

(each χ^2 is given the same weight) gives a tighter constraint on the age-A_v parameter space. The combined best-fitting parameters (Z, age (Ma), A_v (mag)) are (0.001, 15, 0.62), (0.004, 20, 0.54), (0.008, 20, 0.54), (0.020, 10, 0.64), (0.040, 15, 0.52) for reduced χ^2 values of 0.853, 0.800, 0.788, 0.792, 0.789.

In conclusion, both stellar synthesis codes give a consistent picture of the global properties of the source galaxy in FORJ0332−3557, although they marginally disagree on details. They both find young stellar populations of <30 Ma and the presence of some dust extinction. Neither the metallicity, nor the IMF can be robustly constrained although SED@ marginally favours $Z = 0.008$. We emphasize that none of the models, at any metallicity and age, can fit the depth of the observed strongly ionized absorption lines. STARBURST99 points to a young stellar population of 8–10 Ma, in the case of an instantaneous burst, and a few tens of Ma, in case of a constant SFR, whereas SED@ models seem to favour slightly older ages (10–20 Ma) for an instantaneous burst. Lastly, STARBURST99 tends to give a better fit of the absorption features than SED@, including interstellar features of course because SED@ uses synthetic stellar spectra whereas STARBURST99 uses observed stellar templates where the MW interstellar absorption features have not been removed. Finally, SED@ over predicts an absorption line Si IIλ 126.5 nm and a P Cygni profile of O Iλ130.22 nm. Finally, the ages derived by stellar synthesis are older than the presence of the He II emission line seems to suggest. This is not contradictory but rather suggests that the two analyses are not sensitive to the same features, which probably come from different regions of the galaxy and may point at a range of ages and multiple star formation episodes.

4.3 Integrated spectral energy distribution and dust extinction

The photometry in optical bands $B_{\rm Bessel}, v_{\rm Bessel}, R_{\rm Cousin}, i_{\rm Gunn}$, and in infrared bands $J_{\rm S}, H$ and $K_{\rm S}$ is described in Cabanac et al. (2005), Valls-Gabaud et al. (2006). Because the deflector is compact in the optical range, the source $R_{\rm Cousin}$ and $i_{\rm Gunn}$ magnitudes were simply extracted in an annulus of inner/outer radii of 1.5/3 arcsec. The source is faint in $B_{\rm Bessel}$ and $v_{\rm Bessel}$ bands, and we can only put an upper limit to its flux in these bands. The IR magnitudes are more difficult to extract because the foreground deflector covers part of the source. We subtracted the central lens with GALFIT (Peng et al. 2002), using the best-fitting parameters of Cabanac et al. (2005). The derived IR magnitudes are sensitive to the lens subtraction and we estimate that the systematic errors are of the order of 0.3 mag. We obtain the integrated SED (in Vega magnitudes) as shown in Fig. 7.

We derived dust extinctions A_v, and ages of the stellar populations using HYPERZ (Bolzonella, Miralles & Pelló 2000), for the known redshift of 3.7723, an extinction law similar to the SMC and

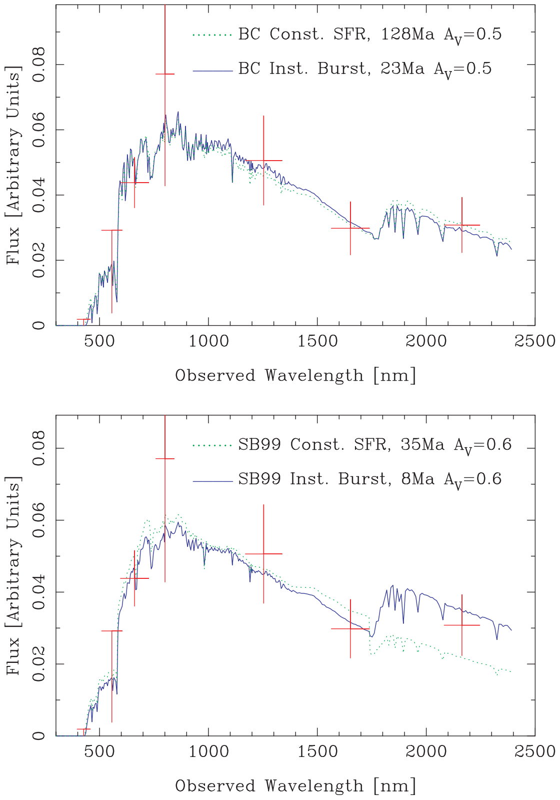

Figure 7. The *BVRIJHK*$_{\rm S}$ SED of FORJ0332−3557 (red crosses, the vertical bars indicating systematic errors and the horizontal ones giving the spectral bandwidth of each filter). The top frame shows HYPERZ best-fitting solar metallicity templates: single-burst template of age 23 Ma (blue solid line) and constant SFR followed by passive evolution template of age 128 Ma (green dotted line). Both templates are the best fits with an extinction $A_v = 0.5$ mag. The bottom frame shows HYPERZ best fit with STARBURST99 $Z = 0.004$ templates: instantaneous burst of age 8 Ma (blue solid line) and constant SFR of age 35 Ma (green dotted line), both with a best-fitting extinction of $A_v = 0.6$ mag. The bottom frame shows a clear difference between a constant SFR and an instantaneous burst near the 400 nm break. We can favour an instantaneous burst scenario based on $K_{\rm S}$ band data.

several libraries of HYPERZ templates, spanning single burst to constant SFR. The stellar initial mass function (IMF) is that of Miller & Scalo (1979) and the metallicity of HYPERZ templates is fixed at the solar value. Although it is likely that FORJ0332−3557 has a subsolar metallicity at a look-back time of ∼12 Ga, at face value solar metallicities are as good a guess as subsolar metallicities. In order to estimate the effect of metallicity on A_v, we also fed HYPERZ with the best-fitting STARBURST99 templates (cf. previous section) of $Z = 0.004$.

Both Single-burst and Irregular HYPERZ templates yield the same dust extinction $A_v = 0.5$ mag (for $R_v = 3, E[B - v] = 0.17$) for the best-fitting 23-Ma-old single-burst template and the best-fitting 128 Ma constant SFR template (Fig. 7). The ages of the stellar populations are not well constrained by stellar synthesis, and Fig. 7 illustrates this point. One template is 100 Ma older than the other and yet they are indistinguishable with broadband data only. The inferred colour excess of $E(B - v) = 0.17$ is similar to the value found by Shapley et al. (2003) (0.169 ± 0.006) for Group 1 (Lyα deficient) LGBs, using a similar extinction law and photometric bands, but a 300-Ma-old constant SFR. FORJ0332−3557 also falls in the middle of the extinction distribution of the $z \sim 4$ LBG sample Steidel et al. (1999).

Following Pettini et al. (2000), we infer the extinction at 150 nm, A_{150} and the H I content, N(H I). For an SMC like extinction law, $A_{150} = 12.6\ E(B - v) \simeq 2$–2.5. Assuming gas-to-dust ratios of $\langle N(\mathrm{H\,I})/E(B-V)\rangle = 4.93 \times 10^{21}\ \mathrm{cm^{-2}\,mag^{-1}}$ for the MW, 1–$2 \times 10^{22}\ \mathrm{cm^{-2}\,mag^{-1}}$ for LMC, and $5 \times 10^{22}\ \mathrm{cm^{-2}\,mag^{-1}}$ for the SMC, we find $7.6 \times 10^{20}\ \mathrm{cm^{-2}} < N(\mathrm{H\,I}) < 10^{21}\ \mathrm{cm^{-2}}$ (MW), $1.5 \times 10^{21}\ \mathrm{cm^{-2}} < N(\mathrm{H\,I}) < 4 \times 10^{21}\ \mathrm{cm^{-2}}$ (LMC) and $7.5 \times 10^{21}\ \mathrm{cm^{-2}} < N(\mathrm{H\,I}) < 10^{22}\ \mathrm{cm^{-2}}$ (SMC). The column density inferred from the Lyα absorption line is compatible with the first two values and would be inconsistent with an SMC gas-to-dust ratio.

4.4 Dust-corrected star formation rate

The UV (150 nm) luminosity is a standard indicator of (massive) star formation. Without correcting for dust extinction and assuming a constant SFR, Cabanac et al. (2005) derived $\mathrm{SFR_{UV}} \approx 31(A/12.9)^{-1}\,h_{70}^{-2}\,\mathrm{M_\odot\,a^{-1}}$, where A is the gravitational amplification produced by the lens. Using the extinction measured in the previous section, $A_{150} = 2$–2.5, we get $\mathrm{SFR_{UV}} \approx 196$–$310(A/12.9)^{-1}\,h_{70}^{-2}\,\mathrm{M_\odot\,a^{-1}}$. Using the same method on cB58, Pettini et al. (2000) derives $\mathrm{SFR_{UV}} = 395\,\mathrm{M_\odot\,a^{-1}}$ (for $H_0 = 70\,\mathrm{km\,s^{-1}\,Mpc^{-1}}, q_0 = 0.1$). This puts FORJ0332−3557 in a very dynamic star-forming episode, similar to what is observed in SDSS J1147−0250 (Bentz, Osmer & Weinberg 2004).

5 CONCLUSIONS

We have presented a medium-resolution spectrum of FORJ0332−3557, a lensed $z = 3.7723 \pm 0.0005$ starburst galaxy, magnified 13 times, very similar to both $z = 2.73$ cB58 and the composite spectrum of LBGs at $z \sim 3$.

We find spectral signatures of outflows of $\sim 270\,\mathrm{km\,s^{-1}}$, commonly found in starburst galaxies, through a distinct residual Lyα emission off-centred by 0.5 arcsec and peaking at ca. $+830\,\mathrm{km\,s^{-1}}$. This offset emission is most probably produced by the outflow rather than by an isolated, bright H II region within the galaxy.

By combining visible-to-infrared colours and spectral features, we derive consistent ages of $\lesssim 10$ Ma for single bursts and 20–40 Ma for constant SFRs and an extinction of $A_v = 0.5$ using two independent stellar populations synthesis codes. Young stellar ages are also supported by the detection of the Wolf–Rayet He II λ164.04 nm line, indicator of stellar ages in the range 4–6 Ma. There is a clear trend to subsolar metallicities in both cases. The ongoing rate of star formation, computed from the 150 nm continuum is $\mathrm{SFR_{UV}} \approx 200$–$300\,h_{70}^{-2}\,\mathrm{M_\odot\,a^{-1}}$.

We also derive preliminary lower limits to the abundances of some the low-ionization interstellar lines suggesting subsolar metallicities in the ionized gas phase.

ACKNOWLEDGMENTS

We are grateful to Max Pettini for providing the spectrum of MS1512−cB58 and important suggestions, Miguel Cerviño for computing a complete set of SED@ templates, Lise Christensen for useful discussions and the anonymous referee for stimulating comments.

REFERENCES

Ando M., Ohta K., Iwata I., Watanabe C., Tamura N., Akiyama M., Aoki K., 2004, ApJ, 610, 635

Asplund M., Grevesse N., Sauval A. J., 2005, in Barnes T. G., Bash F. N., eds, ASP Conf. Ser. Vol. 336, Cosmic Abundances as Records of Stellar Evolution and Nucleosynthesis. Astron. Soc. Pac., San Francisco, p. 25

Bentz M. C., Osmer P. S., Weinberg D. H., 2004, ApJ, 600, L19

Berger E., Penprase B. E., Cenko S. B., Kulkarni S. R., Fox D. B., Steidel C. C., Reddy N. A., 2006, ApJ, 642, 979

Bolton A. S., Burles S., Koopmans L. V. E., Treu T., Moustakas L. A., 2006, ApJ, 638, 703

Bolzonella M., Miralles J.-M., Pelló R., 2000, A&A, 363, 476

Buzzoni A., 1989, ApJS, 71, 817

Cabanac R. A., Valls-Gabaud D., Jaunsen A. O., Lidman C., Jerjen H., 2005, A&A, 436, L21

Cabanac R. A. et al., 2007, A&A, 461, 813

Castelli F., Kurucz R. L., 1994, A&A, 281, 817

Cerviño M., Luridiana V., 2004, A&A, 413, 145

Cerviño M., Mas-Hesse J. M., 1994, A&A, 284, 749

Cerviño M., Valls-Gabaud D., 2003, MNRAS, 338, 481

Cerviño M., Valls-Gabaud D., Luridiana V., Mas-Hesse J. M., 2002, A&A, 381, 51

Cerviño M., Luridiana V., Pérez E., Vílchez J. M., Valls-Gabaud D., 2003, A&A, 407, 177

Dow-Hygelund C. C. et al., 2005, ApJ, 630, L137

Fynbo J. P. U. et al., 2006, A&A, 451, L47

Leitherer C. et al., 1999, ApJS, 123, 3

Miller G. E., Scalo J. M., 1979, ApJS, 41, 513

Noll S. et al., 2004, A&A, 418, 885

Peng C. Y., Ho L. C., Impey C. D., Rix H., 2002, AJ, 124, 266

Pettini M., Steidel C. C., Adelberger K. L., Dickinson M., Giavalisco M., 2000, ApJ, 528, 96

Pettini M., Rix S. A., Steidel C. C., Adelberger K. L., Hunt M. P., Shapley A. E., 2002, ApJ, 569, 742

Savaglio S., Panagia N., Padovani P., 2002, ApJ, 567, 702

Schaerer D., 2003, A&A, 397, 527

Schaerer D., Pelló R., 2005, MNRAS, 362, 1054

Schaerer D., Vacca W. D., 1998, ApJ, 497, 618

Schaerer D., Verhamme A., 2008, A&A, 480, 369

Shapley A. E., Steidel C. C., Adelberger K. L., Dickinson M., Giavalisco M., Pettini M., 2001, ApJ, 562, 95

Shapley A. E., Steidel C. C., Pettini M., Adelberger K. L., 2003, ApJ, 588, 65

Spitzer L., 1978, Physical Processes in the Interstellar Medium. Wiley-Interscience, New York

Steidel C. C., Adelberger K. L., Giavalisco M., Dickinson M., Pettini M., 1999, ApJ, 519, 1

Steidel C. C., Pettini M., Adelberger K. L., 2001, ApJ, 546, 665

Valls-Gabaud D., 1993, ApJ, 419, 7
Valls-Gabaud D., Cabanac R., Lidman C., Diego J. M., Saha P., 2006, in Mamon G. A., Combes F., Deffayet C., Fort B., eds, EAS Publ. Ser. Vol. 20, Mass Profiles and Shapes of Cosmological Structures. EDP Sciences, Les Ulis, p. 149
Vázquez G. A., Leitherer C., 2005, ApJ, 621, 695
Verhamme A., Schaerer D., Maselli A., 2006, A&A, 460, 397
Vreeswijk P. M. et al., 2004, A&A, 419, 927
Vreeswijk P. M. et al., 2006, A&A, 447, 145

This paper has been typeset from a TEX/LATEX file prepared by the author.